Thrust Measurements Using Laser Interferometry

Edward A. Cubbin

April 29, 1998

Thrust Measurement Using Laser Interferometry

by

Edward Andrew Cubbin

Princeton University

School of Engineering and Applied Sciences

Department of Mechanical and Aerospace Engineering

Submitted in partial fulfillment of the requirements for the degree

of Master of Science in Engineering from Princeton University, 1998

Prepared by:

_____

Edward A. Cubbin

Approved by:

_____   _____

Professor Robert G. Jahn   Professor Edgar Choueiri

Thesis Advisor   Thesis Reader

June 1998

Abstract

An optical interferometric proximeter system (IPS) for measuring thrusts and impulse bits of pulsed electric thrusters, has been developed. Unlike existing thrust stands, the IPS-based version offers the advantage of a *single* system that can yield EMI-free, high accuracy ($< 2\%$ error) thrust measurements within a very wide range of impulses (100 μN-s to above 10 N-s) covering the impulse range of all known pulsed plasma thrusters. In addition to pulsed applications, the IPS is theoretically shown to be capable of measuring *steady-state* thrust values as low as 20 μN. The IPS-based thrust stand relies on measuring the dynamic response of a swinging arm using a two-sensor laser interferometer, with $<$10 nm position accuracy for all frequencies. The wide application of the thrust stand is demonstrated with thrust measurements of an ablative pulsed plasma thruster (APPT) and a quasi-steady magnetoplasmadynamic thruster (MPDT). Subsequent to the work presented here, an IPS based thrust stand was permanently installed at the NASA Jet Propulsion Laboratory.

Contents

Acknowledgements

While working toward this thesis, the history and character of Princeton University enriched me more then I had realized. The most vivid impressions come from the people that I met. It was my immediate pleasure to be a student of Professor Robert Jahn: a man capable of profound conversation regarding almost any subject. Professor Edgar Choueiri- Eddie- at first was my lab manager and is now my friend, I am proud to say. I still never saw your attic, Eddie. John Ziemer, Paolo Gessini and I arrived together in the summer of 1994. We soon made our first pasta dinner with many more to come, including several in Eddie's house- the original version. Thank you John and Paolo for the many late nights of work and the great times. The rubber stopper, the D-bar, driving in my Camero. Other veterans of the lab include Waldo Von Jaskowski, George "the Man" Miller, Kevin Diamant, and Vincent Chiravalle. The thinking sessions and lunch time escapes were priceless. Beverly Grosso- I have never met such a bright and wonderful woman as you. You and your thoughts continue to inspire me. My family: Mom, Dad, Dr. Jerry, Diane, and Luci- you all supported me constantly, no matter what, and I needed that. I'll do the same for all of you.

Chapter 1

Introduction to Thrust Measurement

1.1 The Need for the IPS

The performance of many steady-state electric thrusters improves as the operating power level is increased. Due to the limited available power for most foreseeable space missions, instantaneous pulsed high power provides better performance while requiring low average power levels. The ablative pulsed plasma thruster (APPT) is currently the only demonstrated high specific impulse ($>$ 1000 s) propulsion option on small spacecraft with available power levels less than 200 W. This device is described in Ref. [1]. The mass savings advantage pulsed plasma thrusters offer to many near-term power-limited small satellites[2, 3] has renewed interest in these devices and consequently in the accurate measurement of their performance. The most critical performance measurement is that of thrust.

Aside from such thrusters, there is a need to study the performance of quasi-steady magnetoplasmadynamic thrusters (QS-MPDTs). QS-MPDTs were originally used in the laboratory as a simulation of steady-state high power thrusters[4], intended for more futuristic high-power (MW-level) missions[5, 6]. With improved energy storage technology, QS-MPDTs have since been considered as a promising propulsion option in their own right. For such thrusters the requirement is not only

to measure the total impulse but also to resolve the instantaneous thrust *during* the pulse in order to estimate the equivalent steady-state thrust. This is especially crucial when the current pulse used for steady-state simulation differs from a perfect rectangular pulse. This is often the case when using a real pulse forming network (PFN)[7, 8].

Although diagnostic methods already exist for impulse bit and instantaneous thrust measurements of various magnitudes, no *single* high-accuracy diagnostic is known to measure impulse values throughout the entire operating range of typical pulsed plasma thrusters (PPTs), and resolve the thrust of quasi-steady pulsed plasma devices[9]. The needed position measurement accuracy for determining time resolved acceleration can easily be calculated. The QS-MPDTs generate 100 N quasi-rectangular thrust pulses about 1 ms long. Capturing features of the pulse-form that deviate from an ideal square wave (amplitude=100 N and period=2×1 ms) requires measuring acceleration fluctuations that are 10% of the peak thrust value on time scales that are 10% of the pulse period. The typical mass of the thruster is about 20 kg. Considering this higher frequency lower amplitude component of the acceleration

$$a(t) = \frac{10 \text{ N}}{20 \text{ kg}} \sin\left(\frac{2\pi t}{2 \times 10^{-4}}\right), \tag{1.1}$$

the corresponding position fluctuation amplitude is

$$\delta x = \frac{10 \text{ N}}{20 \text{ kg}} \left(\frac{2 \times 10^{-4}}{2\pi}\right)^2 = 0.5 \text{ nm} \tag{1.2}$$

An optical interferometric proximeter system (IPS) was designed to meet these needs (see Section 4.4.3) while providing other advantages. While the motivation for this work was measuring the performance of pulsed *plasma* thrusters, the resulting system and methods are applicable in general for any device that generates an impulsive force.

The IPS thrust stand was designed to accurately measure ($< 2\%$ error) impulse bits for existing practical pulsed plasma thrusters within the range of 100 μN-s

2

to 10 N-s. It is also capable of measuring low steady state thrust down to below 20 μN. This thesis addresses thruster performance measurement fundamentals, the IPS design and operation, experimental results obtained with the IPS based thrust stand, and a full error analysis.

1.2   Review of Previous Work

In the past, impulse and instantaneous thrust measurement systems typically used either an inductive proximeter[10, 11], an accelerometer[7, 8], a linear voltage differential transformer (LVDT)[12, 13], a differential plate capacitance system[14], or an optical angular readout[15]. All included mounting the thruster on some type of thrust arm that was free to move, or swing, in response to an applied thrust. The most sensitive of these past devices appears to be that from Ref. [15], designed in 1968 at NASA JPL, which can measure thrust as low as 5 μN with loads up to 12 kg. A comparable thrust stand was designed at Goddard Space Flight Center in 1970 which measured thrust as low as 25 μN and measured thrust stand deflection as low as 25 nm[14]. Larger thrust and impulse bit measurements have been made as well. A 5 N thrust stand was developed by Haag[16] at NASA Lewis Research Center in 1989 and impulse bits of approximately 1 N-s have been measured at Princeton University[7, 4].

All of these systems assumed that the thrust stand behaved as either a free mass or damped spring-mass system. Except for the accelerometer method, all of the thrust measurement techniques required a spring constant calibration measurement to be performed [4, 7, 8, 12, 14, 15, 16]. This was usually done just before and just after the thrust was applied to be sure that the spring constant did not change due to thermal effects. This type of calibration required a system that could be placed in vacuum tanks and operated remotely. It also had to be non-intrusive to the thrust measurement. The capabilities of the above mentioned thrust measurement

Instrument	Impulse Bit , < 100 μN-s Δ t=1 μs	Time Resolved Acceleration (1 m/s^{2}or 0.5 nm at 5 kHz)
Inductive proximetry probe	Yes	No
Accelerometer	No	Yes
LVDT	Yes	No
Differential plate capacitor	Yes	No
Optical angular readout	No	No
IPS	Yes	Yes

Table 1.1: Thrust Measurement Device Capability

devices are summarized in table 1.2. The IPS is the only device that meets both needs.

1.3 Thrust Measurement Fundamentals

1.3.1 Thrust and Impulse Bit

Performance measurements for a given thruster will rely on one of two different values: the total impulse or the instantaneous thrust. Both are done by analyzing the thrust stand dynamics. A swinging arm type thrust stand is used in our experiments and is described in appendix B. Impulse bit measurements require measuring the thrust stand dynamics before and after the delivered impulse. Instantaneous thrust measurements require measurements *during* the thrust.

1.3.2 Dynamics Models

Damped Spring-Mass Models

Thrust stand systems can be treated like a "black box." The input to the system is the applied thrust and the response of the system can be observed from many locations within the thrust stand system. The exact dynamic response of each observation point on a thrust stand to a given thrust input can, in general, be complicated. Before specific cases are considered, note that the general model for

4

a linear system is

$$x(t) = \int_0^t f(\tau)h(t-\tau)d\tau, \tag{1.3}$$

where $x(t)$ is some observation data, $h(t)$ is the unit impulse response, and $f(t)$ is the applied thrust. This is not of any use until $h(t)$ has been identified for the system. Fortunately, in many cases the thrust stand can be modeled with a high degree of accuracy as a damped spring-mass system. If the motion of the observation point is characterized by x, and the effective natural frequency, damping constant, and mass are $\omega_{n,eff}$, ζ_{eff}, and m_{eff} respectively, an applied impulse bit (I_{bit}) will force the response[17]

$$x(t) = e^{-\zeta_{eff}\omega_{n,eff}t}\frac{I_{bit}/m_{eff}}{\omega_{n,eff}\sqrt{1-\zeta^2}}\sin\left(\sqrt{1-\zeta^2}\omega_{n,eff}t\right), \tag{1.4}$$

where it has been assumed that the system is initially at rest. The duration of the impulse must be much less then the natural period of the observation point for Eq. 1.4 to be valid. In many such cases, measurements can be made on time scales where the effects of the spring and damper are negligible. In the absence of a spring and damper, this model leads to the simple momentum equation,

$$I_{bit} = m_{eff}\Delta\dot{x}, \tag{1.5}$$

where $\Delta\dot{x}$ is the change in velocity of the observation point from before to after the impulse.

If the duration of the thrust (T) is longer then the observation time then Eq. 1.3 becomes

$$x(t) = \frac{T}{m_{eff}\omega_{n,eff}^2}[1 - e^{-\zeta_{eff}\omega_{n,eff}t}[\frac{\zeta_{eff}}{\sqrt{1-\zeta^2}}\times$$
$$\sin\left(\sqrt{1-\zeta^2}\omega_{n,eff}t\right) + \cos\left(\sqrt{1-\zeta^2}\omega_{n,eff}t\right)]]. \tag{1.6}$$

On short time scales, Eq. 1.6 becomes Newton's equation,

$$\ddot{x} = T/m_{eff}, \tag{1.7}$$

5

where $\ddot{x}$ is the acceleration of the observation point and T is the instantaneous thrust. As time becomes large, Eq. 1.6 becomes

$$x(t) = \frac{T}{m_{eff}\omega_{n,eff}^2} = \frac{T}{k_{eff}}, \qquad (1.8)$$

where k_{eff} is the effective spring constant. Whether the appropriate model is this simple or not, the position coordinate provides the dynamic response of the system to an excitation. The IPS was designed around this idea and can accurately provide continuous position data with a resolution better then 10 nm.

System Characteristic Parameters

Historically, a damped spring-mass system has been found to provide an accurate model of the system[12, 7, 8, 15, 4, 16, 14], but these parameters do not always remain steady in an experimental setting. For instance, temperature effects can cause the spring constant, k_{eff}, to change from experiment to experiment. Typically, k_{eff} is measured periodically throughout an experimental session. Unfortunately, this requires a calibration device to be remotely operated, usually inside of a vacuum chamber. With k_{eff}, a steady state thrust can be determined using Eq. 1.8. However, the need for this calibration device can be eliminated.

A damped spring-mass system is characterized by three independent parameters: $\omega_{n,eff}$, and ζ_{eff}, m_{eff}. For instance, the right hand side of Eq. 1.6 is written in terms of the four parameters $\omega_{n,eff}$, ζ_{eff}, t, and T/m_{eff}. The left hand side is measured by the IPS. If, for instance, four position measurements are made at different times during the transient, four different equations can be written. Curve fitting basically does this numerically; many equations are used and solutions for the parameters are found numerically that satisfy all the equations as well as possible. This provides a convenient filtering process to neglect extraneous high frequency vibrations on the thrust stand.

These solutions, however, depend on the ratio T/m_{eff} (or I_{bit}/m_{eff}) and therefore T (or I_{bit}) cannot be obtained with this method alone. A seperate determination

6

is therefore required.

In principle m_{eff} can be determined from

$$m_{eff} = \frac{k_{eff}}{\omega_{n,eff}^2},$$

(1.9)

where $\omega_{n,eff}$ comes from the data fit described above and k_{eff} from direct measurement such as that described above. However, k_{eff} can easily change due to thermal effects. It is therefore better to determine m_{eff} in a seperate experiment by applying a simulated input to the system and observing the dynamic response. This is discussed in section 3.3.1. Note that the thermal effects are implicitly accounted for in the determination of $\omega_{n,eff}$ from the curve fitting process.

Chapter 2

IPS Design Description

2.1   Design Overview

The IPS is based on the Michelson interferometer[18]. The optical nature of this system is one essential feature that solves the electromagnetic interference (EMI) problem common to high current PPTs. Another essential feature is the high spatial resolution capability of optical interferometry.

Fig. (2.1) shows a schematic of the IPS. Light emitted from the laser source is split into two beams at the beam splitter. At the end of each path is a corner cube. The two beams are reflected back to the beam splitter and passed through a lens to the diode sensors. The diode sensor output signals are recorded on a computer. Multiple fringes are facilitated by slightly offsetting the two beams at the diode sensors. When the path lengths traversed by the two beams differ by a non-integer multiple of the wavelength of the laser light (λ) there is a phase angle difference (ϕ) between them when they are reunited. Superposition of these two waves yields constructive or destructive interference. If only one corner cube is allowed to move, then it can be shown that the intensity of light (I) at a particular location on the diode array is related to the relative position (x) of the corner cube by (see appendix A),

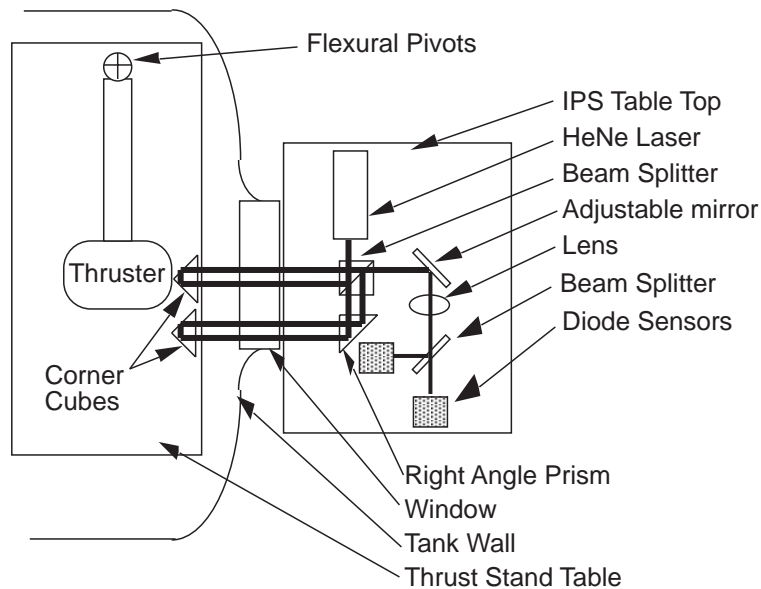$$I(t) = \frac{I_{max}}{2}\left[1 + \cos\left(\frac{4\pi x(t)}{\lambda}\right)\right]. \tag{2.1}$$

Figure 2.1: IPS layout

Eq. 2.1 shows that if $\dot{x}$ is constant, $I(t)$ will appear as an oscillating function with a constant frequency, ω_{IPS}, of

$$\omega_{IPS} = \frac{4\pi\dot{x}}{\lambda}. \tag{2.2}$$

The frequency of the IPS output signal increases with the velocity of the observation point. The corner cubes could also both be mounted on the thrust stand arm. The measurement represents the relative motion between the two points on the arm where the cubes are mounted. This has the advantage of "scaling down" the motion. In either case, the dynamic motion of the thrust stand can be observed via the fringe pattern.

Two diode sensors are used because there are two disadvantages to using a single diode sensor to monitor the fringe pattern. From Eq. 2.1, the position can be obtained by properly taking the arccosine of the intensity signal. The first disadvantage of this technique is that the sensitivity of the cosine function goes to zero at maximum and minimum light intensities. In other words (again consider

9

Eq. 2.1) if the intensity is at a maximum when a change in x occurs, the result is a relatively small change in the light intensity. Compare this to the case when the light intensity level is between a maximum and a minimum in which case the resulting change of light intensity is much larger and quite linear with x.

A second disadvantage to using a single diode sensor to monitor position is that direction reversals can sometimes go undetected. When x is a half integer multiple of λ, I is at a maximum. No matter which way x changes from this point in time, the intensity will diminish, thus direction ambiguity can occur. Both of these disadvantages can be eliminated by using a double diode sensor.

In order to use the double diode sensor, the interference pattern at the diode sensors should not be uniform. This can be achieved by several different methods. For example, offsetting the two interfering beams will result in fringes similar to those in Young's double slit experiment[18]. In this case, as x changes, two given locations within the fringe pattern will change intensity with frequency ω_{IPS} but the resultant cosine curves will be out of phase. By selecting two points within the fringe pattern that are 90 degrees out of phase, there is always one diode sensor output signal in the sensitive region of Eq. 2.1. One way to unfold this double sensor information is to use a scheme called "continuous quadrature." Normalizing the two outputs and plotting one signal versus the other will produce data which fall on the unit circle. In this case the angle corresponding to an arc spanned along this circle is proportional to x. An algorithm can be written which properly takes the arctangent of the data and gives the position versus time. One cycle around the unit circle corresponds to a distance $\lambda/2$. The algorithm must be able to handle many cycles around the circle as well as direction reversals. This technique was coded in LabVIEW 5.0 and used in several experiments. The results are in section 5.1 and 5.2.

2.2 Optics

2.2.1 Optimum IPS Fringe Geometry

Controlling fringe geometry is necessary for basic operation of the IPS as well as maximizing the signal to noise ratio. This is accomplished by properly offsetting, magnifying, and directing the two laser beams before they reach the photo diodes. The components of Fig. 2.2 must be adjusted to produce a fringe pattern which is similar to that in Young's double slit experiment. The separation distance (d) of the two beams can be controlled to produce an optimum fringe pattern at the photo diodes.
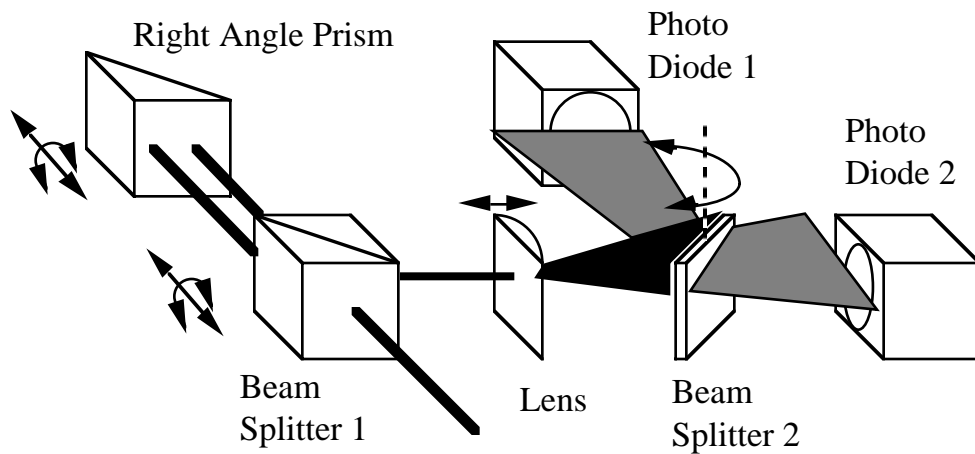

Figure 2.2: IPS Adjustable Components

Maximum Visibility

Visibility is a term commonly associated with interferometers and is usually defined as the ratio of the maximum measured signal to the minimum. Here, visibility (V) is defined as the *difference* between the maximum and minimum, not the ratio. This difference becomes a voltage difference at the photo diode outputs and will be compared to background electronic noise for a signal to noise ratio calculation. The width of a fringe (δ) relative to the photo diode can can be optimized to give

the greatest visibility. Consider a sensor of width l centered on a fringe pattern as depicted in Fig. 2.3. The cylindrical lens (see Fig. 2.2) expands the light in the horizontal dimension and the diode sensor area has a vertical height greater then that of the resulting laser sheet. It is assumed that the beam width, b, is much greater then the beam separation distance, d. The maximum integrated intensity measurement will occur when the sensor is centered on a bright region of a spatially harmonic intensity distribution, $I(\xi)$, which is given by

$$I(\xi) = \frac{P}{b}\left(\frac{1}{2} + \frac{1}{2}cos\frac{2\xi\pi}{\delta}\right),\tag{2.3}$$

where P is the total power of the combined beams, and ξ is the location along the
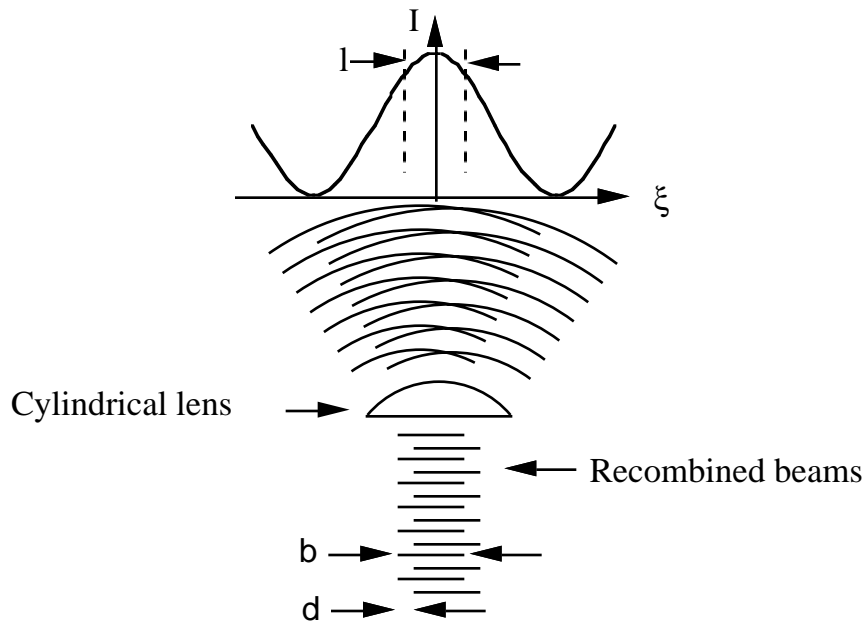

Figure 2.3: Diode Fringe Pattern

fringe pattern. The intensity distribution for two interfering, circular cross section beams with a gaussian intensity distribution is more complicated then Eq. 2.3, but is not necessary for this analysis. Integrating Eq. 2.3 over the length of the sensor

12

gives the maximum integrated intensity measurement (S_{max}):

$$S_{max} = 2\frac{P}{b} \int_0^{l/2} \left(\frac{1}{2} + \frac{1}{2}cos\frac{2\xi\pi}{\delta} \right) d\xi = \frac{P}{b} \left(\frac{l}{2} + \frac{\delta}{2\pi}sin\frac{\pi l}{\delta} \right). \tag{2.4}$$

Similarly, for the minimum integrated intensity measurement (S_{min}) is centered on a dark part of the fringe pattern:

$$S_{min} = 2\frac{P}{b} \int_0^{l/2} \left(\frac{1}{2} - \frac{1}{2}cos\frac{2\xi\pi}{\delta} \right) d\xi = \frac{P}{b} \left(\frac{l}{2} - \frac{\delta}{2\pi}sin\frac{\pi l}{\delta} \right). \tag{2.5}$$

Differencing (S_{max}) and (S_{min}) gives an expression for the visibility (V):

$$V = S_{max} - S_{min} = \frac{P}{b} \left(\frac{\delta}{\pi}sin\frac{\pi l}{\delta} \right). \tag{2.6}$$

It is now clear that the optimum relationship between fringe width δ and photo diode sensor size (l) is

$$l = \frac{\delta}{2}, \tag{2.7}$$

which gives a maximum visibility of

$$V_{max} = \frac{P\delta}{b\pi}. \tag{2.8}$$

Beam Separation Distance

The fringe pattern intensity will have an harmonic spatial distribution similar to Fig. 2.3. The fringe pattern can be predicted by treating each laser beam as a diverging spherical wavefront as in Young's double slit experiment. The fringe width (δ) from the double slit experiment is

$$\delta = \frac{\lambda R}{d}, \tag{2.9}$$

where R is the radius of curvature of the wavefront of the laser beam. The beam width, b, is given by

$$b = R\phi, \tag{2.10}$$

13

where ϕ is the laser beam divergence angle. Combining Eqn. 2.8, 2.9 and 2.10 gives an expression for the maximum visibility:

$$V_{max} = \left(\frac{P\lambda}{d\phi\pi}\right). \tag{2.11}$$

Eq. 2.11 predicts that decreasing d (increasing the fringe widths) yields better visibility. d can be made arbitrarily small but the sensed portion of the interference pattern, l, can be no larger than the width of the entire interference pattern, which is of course limited to the beam width, b. Further, there is a more practical upper bound on δ, and thus on l. Recall that at least 1/4 cycle ($\delta/4$) of an intensity distribution is needed to allow proper placement of the diodes (see section 2.1). This is actually the required distance between center locations of the photo diodes. Considering now that the diode sensors are to have a width of $\delta/2$, the fringe pattern must now contain at least 3/4 of a cycle of fringes, or $3\delta/4$. If the beams of width b are offset by a distance d, the size of the interference region will have width $b - d$. This gives, using Eq. 2.9 and 2.10,

$$b - d = \frac{3}{4}\delta = \frac{3}{4}\left(\frac{\lambda b}{d\phi}\right). \tag{2.12}$$

Solving for (d) after neglecting the second order term:

$$d = \left(\frac{3}{4}\right)\frac{\lambda}{\phi}. \tag{2.13}$$

For a helium neon laser with $\phi = 1.7$ mRad

$$d = \left(\frac{3}{4}\right)\frac{632.8\text{nm}}{1.7\text{mRad}} = 0.37 \text{ mm}. \tag{2.14}$$

This magnitude of positioning is easily achieved with optical translation stages. A larger separation distance will produce more fringes with smaller fringe width (δ). Eq. 2.11 shows that the signal strength will decrease proportionally.

Fringe Pattern Magnification

The interference region will most likely need to be magnified to accommodate the size of the photo diode. The interference region should be 3/4 of a fringe width

14

and the sensor should be 1/2 of a fringe width, which means the interference region should be 3/2 the width of a photo diode sensor. In these experiments, the photo diodes were about 5 mm wide squares. This required a magnification factor of about 4. Such a magnification also facilitates a visual inspection of the fringe pattern, which is the easiest way to determine that it is approximately 3/2 the photo diode width. The magnification is done with a cylindrical lens so that the fringes are made wider then the photo diodes but not taller. This utilizes all of the available light for a better signal to noise ratio.

2.2.2 Phase Difference Misalignment

When the phase difference (ϕ) is not exactly $\pi/2$ a small error in calculating position arises. This error can be corrected, but since it is not cumulative, and repeats every time the path length changes by the laser wavelength, λ, this correction is only needed when motion on scales much less then λ are important. For a phase misalignment of ϕ, one diode output signal (V_a) can be represented (after it has been normalized) as

$$V_1 = \cos(f(t)), \tag{2.15}$$

where $f(t)$ is a function representing the changing path length in the IPS and the second diode output (V_2) is

$$V_2 = \sin(f(t) + \phi). \tag{2.16}$$

For a given set of measurements, (V_1 and V_2), Eqs. 2.15 and 2.16 contain two unknowns: $f(t)$ and ϕ. An equation can be written involving only V_1, V_2, and ϕ:

$$V_1^2 = \frac{\left[\cos(\tan^{-1}(\frac{\frac{V_2}{V_1}-\sin\phi}{\cos\phi}))\right]^2 + \left[\sin(\tan^{-1}(\frac{\frac{V_2}{V_1}-\sin\phi}{\cos\phi} + \phi))\right]^2}{1 + (\frac{V_2}{V_1})^2}. \tag{2.17}$$

Sections of data are used to curve fit for ϕ. Once a value for ϕ is found, all of the V_2 data can be corrected to represent a diode measurement with $\phi = 0$. Eq. 2.16

can be used to produce an expression for the needed data, $\sin x$:

$$\sin x = \frac{V_2 - V_1 \sin \phi}{\cos \phi}. \tag{2.18}$$

Eqs. 2.15 and 2.16 can be used to solve for the actual $f(t)$,

$$f(t) = \tan^{-1} \left(\frac{\frac{V_2}{V_1} - \sin \phi}{\cos \phi} \right). \tag{2.19}$$

The algorithm otherwise used computes $f(t)$ as

$$f(t) = \tan^{-1} \frac{V_2}{V_1}. \tag{2.20}$$

For $\phi = 0.1$ radians, momentary errors of a few nanometers occur in the regular calculation of position.

2.2.3 Corner Cubes: Path Length Geometry

It remains to be shown how the path length of the laser beam changes as the corner cube moves. It is often stated that the path length of a beam reflected by a corner cube depends only on the translational motion of the corner cube along the axis of the beam. In fact, this is only true with a mirrored surface corner cube but not with a prism corner cube.

The key to calculating path lengths through a corner cube is to realize that the path length inside of a corner cube is equal to the distance a beam would travel through an equivalent cube shaped prism (see Fig. 2.4). This equivalent cube has a width equal to twice the depth of the corner cube. Fig. 2.4 shows the 2 internal reflections and an outline of an equivalent cube. It is clear that lengths a and b are equal to lengths b and b'. Therefore, the path length inside of a corner cube is only a function of the incidence angle. With this tool, lateral translation and rotation can be examined.

Lateral Translation

Fig. 2.5 depicts an incoming beam (i) and an exiting beam (e_1) at the external surface of a corner cube. The surface is translated a distance d, perpendicular to
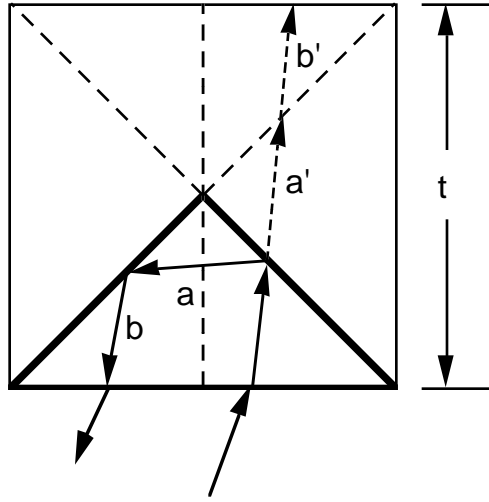
Figure 2.4: Equivalent Cube for Internal Corner Cube Path Length

the beam axis and shown as a dotted line. The new exiting beam (e_2) shifts to
a new position. The translation of the corner cube causes the *relative* location of
beam i to move away from the corner cube center line an additional distance Δ.
The *relative* location of beam e_2 also moves away from the center line an additional
distance Δ. This can be easily deduced from Fig. 2.4. For a fixed incidence angle,
the path length inside of the corner cube will not change. Beam i travels further by
a distance $\Delta \sin \theta_1$. The exit beam e_2 emerges from the surface a distance $\Delta \sin \theta_1$
closer. These sum to zero, proving that lateral translation causes no net path length
change.

Rotation

Fig. 2.4 can be used to show that rotating a mirrored surface corner cube, or a
prism corner cube with index of refraction (n_2) equal to that of the surrounding
medium (n_1), does not change the path length if rotation is performed about the
corner of the corner cube. Such a rotation for $n_2 \neq n_1$ can be investigated using
Fig. 2.6. In Fig. 2.6 a corner cube is rotated about the entrance point P. The
dotted line corner cube configuration provides a baseline path length (L_1) inside of
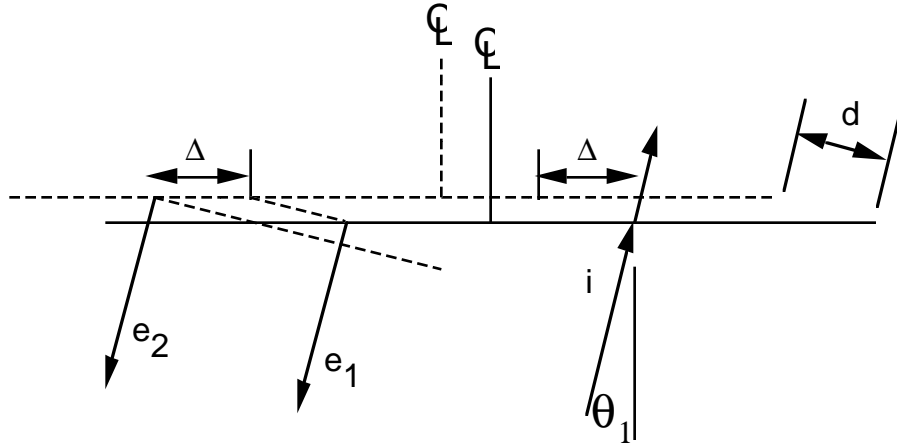
Figure 2.5: Lateral Translation of Corner Cube

the corner cube. The incoming beam enters at point P, reflects at the corner and exits at P. This baseline internal path length is

$$L_1 = tn_2. \tag{2.21}$$

If the corner cube is rotated about P by an angle θ_1, the path length inside of the rotated corner cube is

$$L_2 = \frac{tn_2}{\cos\theta_2}. \tag{2.22}$$

The corner of the corner cube will be used here as the reference point as it is for a mirrored surface corner cube. The rotation causes the corner of the corner cube to move along the axis of the incoming beam by a distance

$$\delta l = \frac{t}{2}\left(1 - \cos\theta_1\right). \tag{2.23}$$

The path length will decrease by twice this value.

The last term to consider is the distance d. The exiting beam emerges a distance d closer to the beam source after rotation:

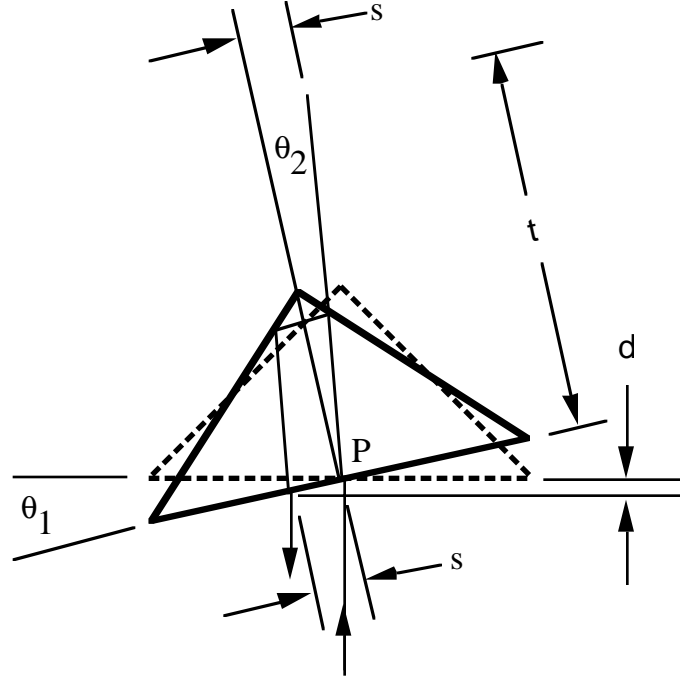$$d = s\sin\theta_1 = (t\tan\theta_2)\sin\theta_1. \tag{2.24}$$

18

Figure 2.6: Rotation of Corner Cube

Assuming that rotation about the corner causes a path length increase ϵ,

$$L_2 + d + \delta l - \epsilon = L_1. \tag{2.25}$$

Solving for ϵ and using Snell's law gives

$$\epsilon = t\left(\frac{n_2}{\cos\theta_2} - n_2 - \frac{n_1^2\sin^2\theta_1}{n_2^2\cos^2\theta_2} + n_1 - n_1\cos\theta_1\right) \approx t\left(\frac{n_1\theta_1^2}{2}\left(1 - \frac{n_1}{n_2}\right)\right). \tag{2.26}$$

For a corner cube location on a thrust arm of length L as shown in Fig. 2.1, the ratio (R) of ϵ to the translational motion along the beam axis is

$$R \approx \frac{t}{L}\left(\frac{n_1\theta_1}{2}\left(1 - \frac{n_1}{n_2}\right)\right). \tag{2.27}$$

For $L = 1$ m, $t = 5$ cm, $n_1 = 1$, $n_2 = 1.25$, and $\theta_1 = 10^{-3}$, $R = 5 \times 10^{-6}$. This is a negligible effect.

19

2.3   Electronics

2.3.1   LabVIEW Data Acquisition Card

There are many cards available for a personal computer that are compatible with LabVIEW. The card used for these experiments had a maximum sample rate of 100 kHz. Also, this card could be triggered from an external trigger source.

2.3.2   Photo Detectors

The photo diodes used for these experiments (see the parts list below) were housed in a casing that also contains an adjustable amplifier. Each output was connected to the LabVIEW card with a coaxial cable.

2.4   Data Acquisition and Processing Software

LabVIEW by National Instruments Corp. is a graphical programming language. When used in conjunction with input/output electronics cards for personal computers, LabVIEW becomes a fully programmable data acquisition and control system. The program, or code, is called a "Virtual Instrument" or VI. Smaller sections of a VI are packaged into smaller subVIs. These subVIs can receive inputs and produce outputs. The programming is called "graphical" because each subVI is represented by an icon on the computer monitor, and lines are drawn between subVIs to represent the exchange of data between them.

2.5   Parts List and Assembly

All of the parts labeled in Fig. 2.1 are shown also here in Fig. 2.7. All components can be purchased from two companies: Edmund Scientific and ThorLabs Inc.

ITEM	CAT	QTY	COST EA. ($)
prism holder	A53030	2	60
rotary translation stage	A38193	2	505
gimbal tilt table	A38929	2	125
twin ring mount	A71791	1	65
HeNe Laser	A61318	1	560
bench plate	A3640	1	295
gimbal mirror mount	A39929	1	118
3" post	A36497	1	10
2" post holder	A3646	1	12
cylindrical lens	A43856	1	99.80
bandpass filter	A30910	2	143.35
HeNe laser mirror	A43533	2	17.15
corner cube	A43297	2	149
beam splitter	A32505	1	130.80
right angle prism	A32336	1	41.10
mirror beam splitter	A45325	1	20.70
			3,351.40 total

Table 2.1: Supplier: Edmund Scientific

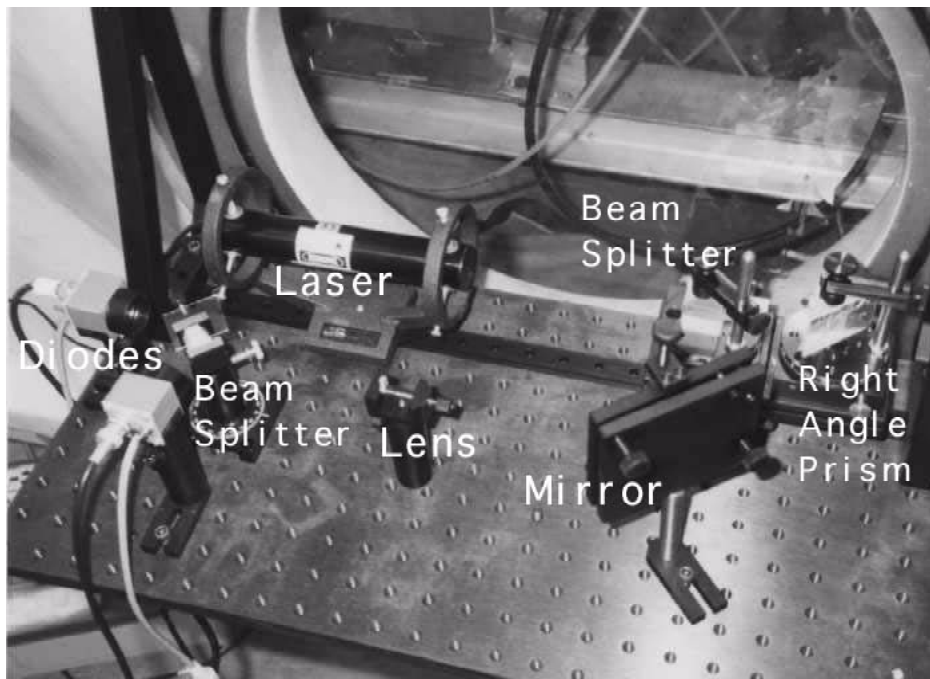| ITEM	CAT	QTY	COST EA. ($)
rail carrier	RC1	3	15
dovetail carrier	RC3	2	23
post shim	PS3	4	8
optical rail	RLA2400	1	99
plate holder	FP01	2	39
2" post	TR2	4	5
3" post holder	PH3-ST	4	12
base	BA1S	3	7.50
photo detector	PDA50	2	268
rotation platform	RP01	1	79
vertical bracket	VB01	2	79
			1,163.50 total

Table 2.2: Supplier: ThorLabs Inc.

Figure 2.7: IPS Picture

Chapter 3

Thrust Measurement Procedure

3.1 Corner Cube Placement

The corner cubes can be located for measuring relative motion or absolute motion. If they are both on the thrust arm, they will both rotate and translate and the relative motion is registered by the IPS. If one corner cube is fixed to a stationary location, absolute motion is detected. In general, it is much easier to work with the IPS measuring small, relative motions. As long as the relative motion is large enough to measure accurately- at least a few wavelengths- less motion requires slower sampling rates and smaller data files.

3.2 Alignment Procedure

The adjustable components of the IPS are shown in Fig. 2.1 and 2.2. The following procedure list should be used to align the IPS for maximum visibility.

- Raise the table approximately to the level of the corner cubes.

- Slide beam splitter 1 and the right angle prism to the approximate positions of the corner cubes.

- Turn on and align the laser such that the beam enters beam splitter 1 approximately in the center.

- Turn and tilt the beam splitter 1 to direct the beam into the corner cube. Be sure that the reflected beam passes again through beam splitter 1.

- Remove then cylindrical lens and adjust the mirror to direct the beam onto photo diode 2.

- Locate the cylindrical lens along the beam path to magnify the beam to a width of about 1.5 times the width of the diode sensor area.

- Use the adjustable mirror to align the right edge of the magnified beam with the edge of the diode sensor, as depicted in Fig. 2.2.

- Turn beam splitter 2 and adjust the height of diode 1 to direct the magnified beam onto photo diode 1 such that, again, the right edge of the beam and photo diode 1 are coincident. Note that the reflection at beam splitter 2 produces a mirror image of the beam pattern.

- Turn and tilt the right angle prism to direct the beam into the corner cube and make it coincident with the other beam image at the photo diodes.

- The output signals should be nearly in phase (monitor them on an oscilloscope). Turn the right angle prism with the fine adjustment screw until the phase difference appears to be approximately $\pi/2$.

- The IPS is now aligned.

3.3   Effective Mass Measurement

3.3.1   Summary of Technique

Once two locations have been chosen for the corner cubes, the effective mass (m_{eff}) must be determined. This process is equivalent to calibrating the IPS based thrust stand. A known impulse must be given to the thrust stand while the response is

recorded by the IPS. The impulse must be applied at the same location as the force which is applied during an actual firing of the thruster. A commercially available force transducer provides a simple way of applying a measurable impulse. The thruster must be struck with the force transducer while the force transducer output voltage is being recorded. Integrating the force with respect to time yields total impulse. The IPS should record the response of the thrust stand to the impulse. From the measured change in velocity (Δv), m_{eff} can be determined using the measured total impulse for I_{bit}:

$$m_{eff} = \frac{I_{bit}}{\Delta v}. \tag{3.1}$$

3.3.2 Impulse Delivery Device

The calibration impulse was delivered by a 30 cm long 0.5 kg steel rod that was used as a pendulum (see Fig. 3.1). The rod pivots on a teflon pin which was fixed to an aluminum stand. This stand was mounted inside of the vacuum tank in front of the thruster. An electromagnet was also mounted on the pendulum stand so that the pendulum could be cocked and then released remotely. Care must be taken to align the pendulum so that the force is delivered along the thrust axis. See section 4.3 for a quantification of this alignment error.

The force transducer used was a model 208A02 Force Transducer from Piezotronics. The operating range is from 0-400 N. A vertical static load was applied to the force transducer to calibrate it in a range of 0-100 N. The resultant calibration constant was found to be 87.6±0.6 N/V. The output signal is recorded during an impact on a Nicolet 320 Digital oscilloscope and then analyzed on a computer. The data was digitally integrated to obtain a value for I_{bit}.
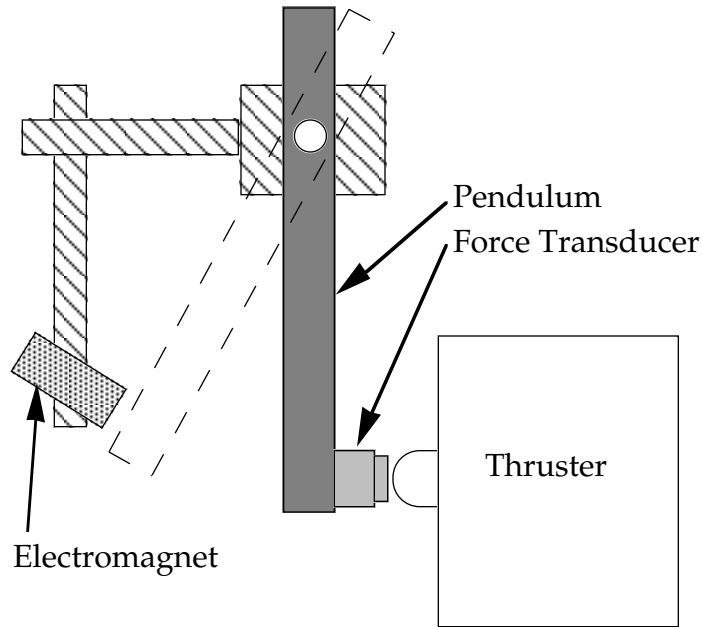
Figure 3.1: Pendulum device for m_{eff} calibration

3.4 Choosing a Dynamic Model: the Power Spectrum Technique

The IPS is capable of measuring position data in many frequency and amplitude regimes. Since the IPS can be used in different ways to measure the same thruster performance value (i.e. Δv measurement, steady state displacement measurement, or damped sinusoidal fit) it is necessary to find a way of choosing the best technique. This can be done by considering the power spectrum of the background noise.

The power spectrum of the background noise can be used to indicate which of the various measurement techniques should be used to obtain a thrust measurement. One must first calculate what ideal response of the thruster arm is expected from the predicted impulse. For instance, for the sinusoidal response, the strength of the signal expected (as in Fig. (5.1)) can be compared to the background noise at the natural frequency of the arm. This will give an estimate of the signal to noise ratio and indicates the accuracy of the IPS for this type of measurement. If needed, a

band-pass filter can be applied to the raw IPS data to eliminate background noise before the curve fitting process is begun. Each technique should be considered and the one with the highest signal to noise ratio will provide the most accurate measurement.

Noise with Stiff Power Connection

When operating the MPDT, the power supply connection used a coaxial conductor built inside the thrust stand arm that connects the thruster on the stand to the capacitor bank. The connection goes through an access window on the tank wall. The transmitted background noise is quite acceptable and is shown in Fig. 3.2. A quantitative evaluation of this typical background position noise can be done by considering the Fourier Transform of the signal. By taking the Fourier Transform and multiplying each point on the curve by the square of its frequency, the power spectrum of *acceleration* is obtained. From this plot (see Fig. 3.3) any particular experiment can be considered. For instance, the MPDT acceleration pulse that is to be measured has an amplitude of $\sim$5 m/s^2 and lasts for 1 ms. This amounts to measuring a 500 Hz, 5 m/s^2 square wave against the noise. Frequencies significantly far from 500 Hz may be filtered out during the experiment and therefore the power spectrum amplitude near 500 Hz in Fig. 3.3 depicts the accuracy allowed for that measurement due to noise.

Noise without Stiff Power Connection

When the capacitor bank is not being used and the rigid power connection to the thrust stand is removed, the background noise is reduced considerably. Figure 3.4 shows the corresponding background noise. It is useful to perform a similar analysis on this data to that done above. In experiments of this kind, acceleration was not studied considering the short pulse duration (10 μs). In this experiment the impulse will provide a damped sinusoidal motion of the thrust arm. Therefore the power
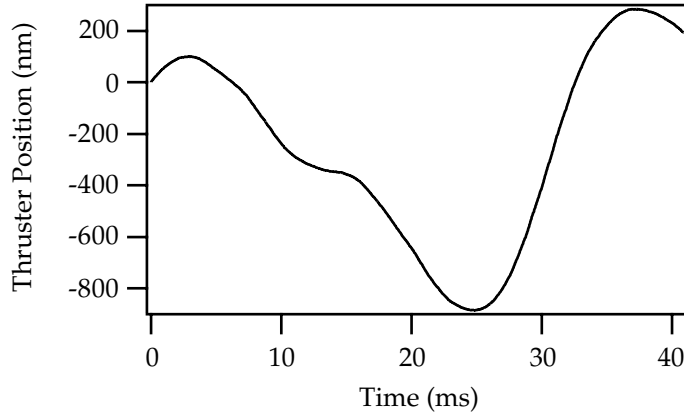
Figure 3.2: Background position noise for MPDT experiments.

spectrum for position should be considered. Figure 3.5 is the Fourier Transform of Fig. 3.4. For this particular case, the natural period of the thruster arm corresponds to a signal frequency of ~ 0.2 Hz and an amplitude of ~ 15 μm. Figure 3.5 shows that the noise at this frequency is small.

3.5 Configuring IPS.vi.5 Software

Several LabVIEW programs(VIs) were created for the IPS. The user interface is shown in Fig. 3.6.

Scan Rate The scan rate should be set based on the expected maximum frequency of the photo diode output. The frequency is related to the expected motion of the corner cubes as expressed in Eq. 2.2 and is repeated below.

$$\omega_{IPS} = \frac{4\pi\dot{x}}{\lambda}. \tag{3.2}$$

Vibrations often require the scan rate to be increased. This is most easily determined experimentally. The LabVIEW software will inform the user if the selected scan rate exceeds the capability of the computer hardware.
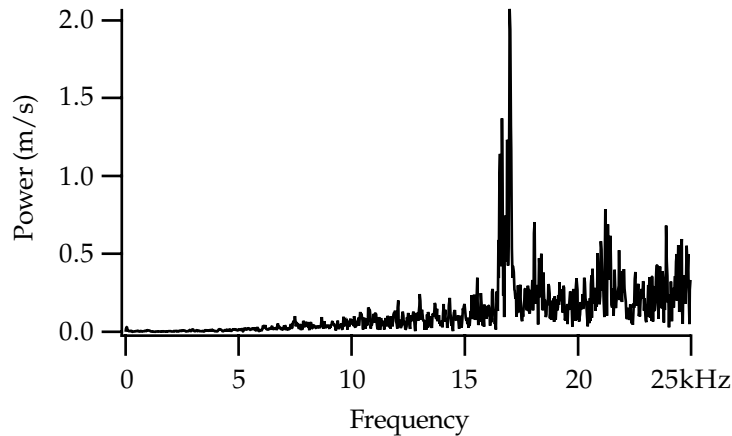
Figure 3.3: Background acceleration power spectrum for MPD experiments.

Memory Time The memory time is entered in seconds. If selected, this much data will be saved to disk.

High Accuracy Mode When this option is selected, the VI Phasefit.vi is used to correct the phase difference between photo diode 1 and 2 to $\pi/2$. This is needed only when displacements of a few nanometers is important.

External Trigger Mode When this is selected, an external trigger signal can be used to begin sampling the photo diode output. Alternatively, the sampling can be started automatically when the VI is set to "run" mode.

Input Voltage Limits Based on the output capability of the photo diode sensors, the voltage limits should be set to slightly more then is expected. It is important not to set these limits too high, because the range will be divided by the A/D converter, and a smaller range yields finer voltage resolution in the measurement.

File Saving Options The calculated position as well as the raw diode data can be saved. The file names contain the trial number that is displayed in the front
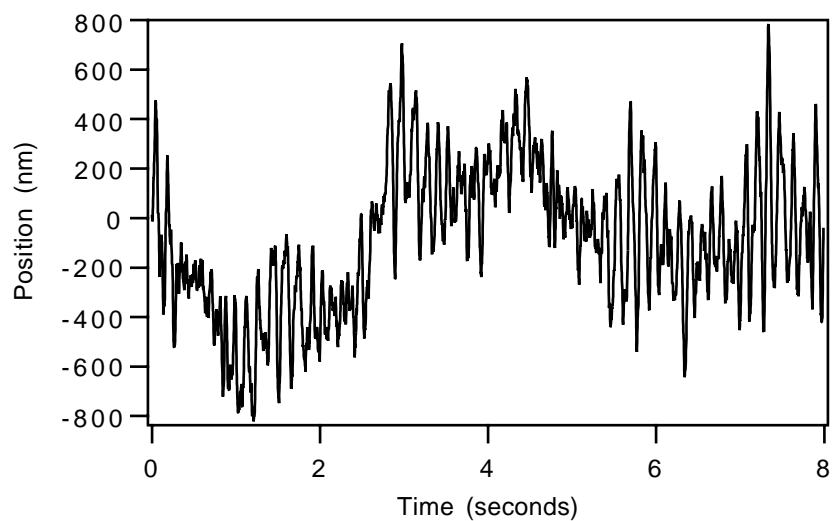
Figure 3.4: Background position noise for APPT experiments.

panel. Since Igor Pro was the software package used for curve fitting and data analysis, the files are saved as Igor binary files. This is easily changed if needed.

Chart Displays The user can select which charts are active. If it becomes time consuming for all of the charts to be generated, any of them can be disengaged.
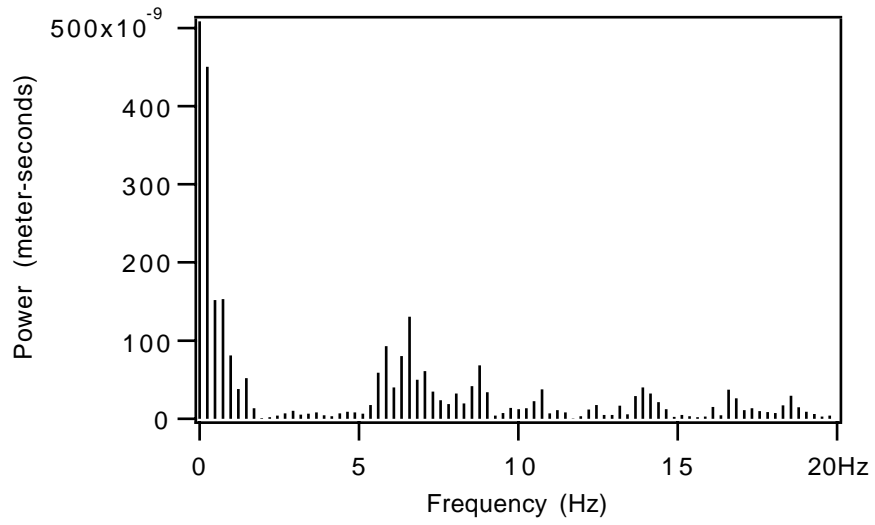
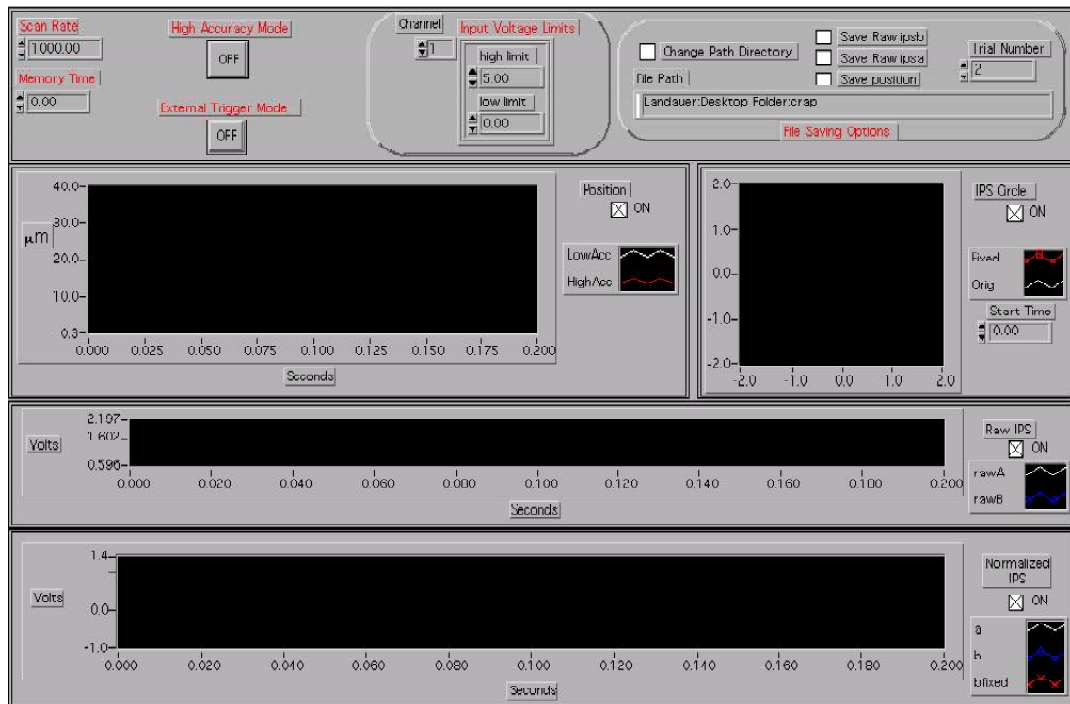Figure 3.5: Background position power spectrum for APPT experiments.

Figure 3.6: User interface panel

Chapter 4

Error Analysis

This section presents an error analysis for the different IPS measurements. First the IPS raw measurement error of 10 nm is experimentally determined. Then the background mechanical perturbations to the system are considered in an error analysis of the impulse bits reported above. Each final impulse value is comprised of a m_{eff} measurement and a value from a curve fit. The m_{eff} error is determined from the accuracy of the force transducer and the estimated experimental error of alignment, and the error associated with the curve fit values is estimated from a statistical approach, again considering the background mechanical noise.

4.1 IPS Position Measurement Accuracy

The IPS position error is established by aiming both beams of the interferometer into the same corner cube. This conservatively reveals the internal noise of the IPS. Fig. 4.1 shows 1 s of noise. The standard deviation on this noise is <10 nm for all frequencies. Figs. 3.2 and 3.3 show <1 nm noise for many shorter time scales.

4.2 Mechanical Isolation of Thrust Stand

Experience showed that position recording instruments in the tank, including the IPS and the proximeter, were easily influenced by normal motion of personnel about the lab. Micron size noise was easily recorded for experiments where the total
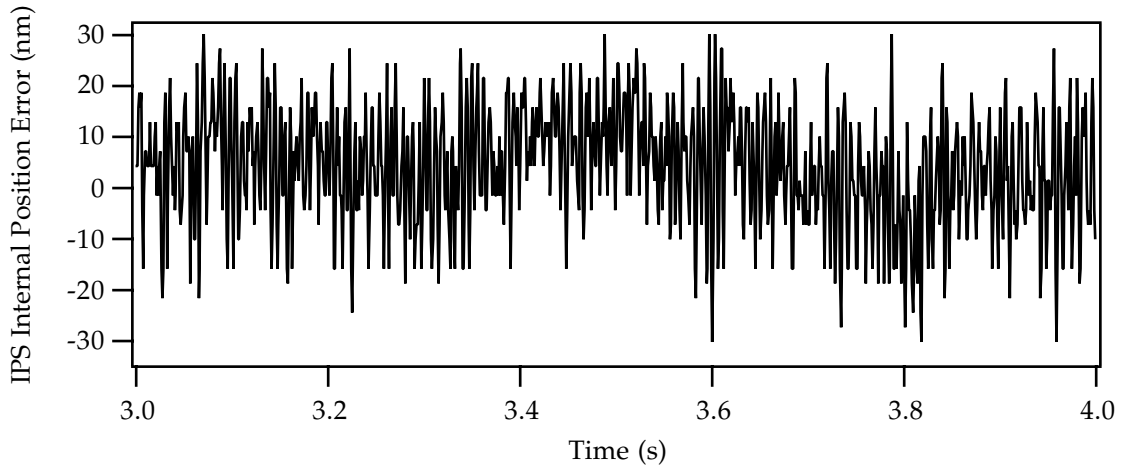
Figure 4.1: Position Noise; Standard Deviation is $\sigma = 10 \ nm$

displacement is about 10 microns. For instance the LES 8/9 APPT displaces a total of 15 microns after a single pulse (see section 5.1). Also, mechanical equipment, including the vacuum pumps provided vibrations of up to 5 microns. As a result of this it was decided that the thrust stand should be mechanically isolated from the lab environment.

4.2.1 Techniques for Mechanical Isolation

Several techniques were considered for mechanical isolation of the thrust stand table. Among the ideas were elastic supports, various commercially available optical bench isolation devices, and suspension. The best available mechanical isolation devices from Oriel Corporation provide a transmissibility of 10^{-3} at a frequency of 60 Hz [19]. According to Oriel Corporation they could not be used in a vacuum environment. However, it appeared that suspension of the table by springs could provide a similar transmissibility curve for the thruster table.

The transmissibility of a one dimensional spring-mass system characterizes the motion of the mass due to base excitation. The ratio of the amplitudes of the mass

33

motion (X) to the base motion (Y) for sinusoidal base excitation is

$$\left|\frac{X}{Y}\right| = \frac{k_{eff}}{k_{eff} - m\omega^2} \tag{4.1}$$

where k_{eff} and ω are the effective spring constant and mass respectively [17]. Suspension by springs can be analyzed as such by considering the vertical and horizontal dimensions separately.

Horizontal Isolation   When the table is suspended by springs it will swing freely in any horizontal dimension like a pendulum. The mass of a pendulum is mechanically isolated from its base. The k_{eff}, in this case, corresponds to the restoring force on the mass. For small angle deflections (θ), a pendulum length (l), and the acceleration of gravity (g)

$$k_{eff} = \frac{mg}{l}. \tag{4.2}$$

The transmissibility is then independent of m and is

$$\left|\frac{X}{Y}\right| = \frac{g/l}{g/l - \omega^2}. \tag{4.3}$$

For $l = 0.5$ and a frequency of 60 Hz

$$\left|\frac{X}{Y}\right| \approx \frac{1}{6500}. \tag{4.4}$$

In the case that all support springs are the same final length and the base excitation is pure translation, the one dimensional model is exact.

Vertical Isolation   For the vertical dimension, k_{eff} is the total spring constant of all of the supporting springs and the m is the mass of the table again. The mass of the table was estimated to be 200 kg. Eqn. 4.1 can be used to compute a required k_{eff} of approximately 30,000 N/m. Several types of commercially available springs were considered including custom made ones. It was found that this k_{eff} can be achieved by using a reasonable combination of inexpensive off-the-shelf springs.

4.2.2 Implemented Spring Support for Mechanical Isolation

The four corners of the thruster table were chosen as the attachment locations for the support springs. Individual initial spring length was determined iteratively. The final length of each spring was to be maximized for horizontal mechanical isolation (see Eqn. 4.3). There is of course a height constraint based on the height of the tank. The number of springs must then be minimized to minimize the final k_{eff}. However, each spring must not yield under the load of the table. The chosen springs were carbon steel 1.5 inch outer diameter (D), 0.162 wire diameter (d) continuous length extension springs. The maximum shear stress (τ_{max}) in a spring loaded with axial force (F) is [20]

$$\tau_{max} = \frac{8FD}{\pi d^3}.\tag{4.5}$$

For τ_{max}= 290 MPa, the maximum axial load for these springs is 230 N. Therefore, based on the predicted weight distribution of the thruster table, three springs were place at the tank door right corner of the table, and two at each other corner. The eyebolts can be raised and lowered to accommodate different table weights avoiding the need to accurately predict an initial spring length for each corner. For all the springs nearest the tank door, an initial length of 22 inches of coils was used. For the back left and right corners, 26 and 23 inches respectively were used .

4.2.3 Alignment Considerations

One potential source of motion within the IPS is that of the IPS table top. The plane of the table top is horizontal. In this case, IPS table top vertical motion and motion parallel to the thruster arm will not change the path length of either beam (see section 2.2.3). However, motion perpendicular to the plane of the window will change the path length in general. A geometric analysis of translational motion of the table top shows that the relative path length difference is a function of the angular alignment of the beams and the magnitude of the table top motion. Using

the symbols shown in Fig. 4.2 and small angle approximations, an expression for this induced path length difference is

$$\Delta L_2 - \Delta L_1 = \Delta x \left(\frac{1}{\cos\theta_2} - \frac{1}{\cos\theta_1} \right) \approx \Delta x \frac{\theta_2^2 - \theta_1^2}{2}. \qquad (4.6)$$
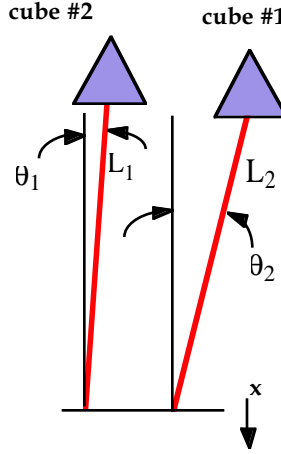

Figure 4.2: Schematic of beam alignment

4.3 Effective Mass

The calibration constant for the force transducer was determined by applying static loads to the load cell and measuring the voltage output. Within the operating range of this experiment, the calibration constant was repeatable to within 0.7% of 87.2 N/V. The integration was done numerically on a computer. The zero level was taken as the average value before the impact (see Fig. 4.3). This value varied much less then 1% of the peak signal strength and was negligible. The integration can be done to an accuracy of 1%.

Another source of error is the alignment of the calibrating pendulum with the thrust axis. If an alignment of 3 degrees is maintained, the error incurred is 0.1%. The pendulum was aligned to this tolerance (verified by geometric measurements) so the incurred error was negligible. The calculated I_{bit} for the quasi-steady MPDT
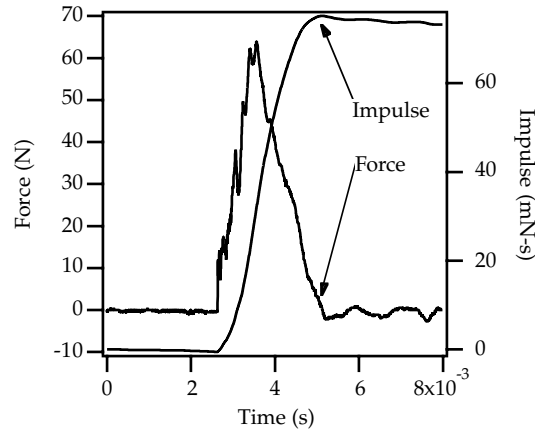
36

Figure 4.3: Force delivered by pendulum and integrated force for total impulse

is linearly depended on m_{eff} (see Eq. 5.3.) Summing the errors identified in this section yields a 1.7% error for the m_{eff} measurement.

4.4 Curve Fitting

4.4.1 A Linear Fit

All of the curve fitting of the data was performed using the software package Igor Pro by WaveMetrics. In the case of the quasi-steady MPDT I_{bit} calculation, $\dot{x}$ was found using a line fit to the position data after the pulse. If the scatter of the data around the fit is considered to be noise, a standard deviation value can be computed for the slope. This computed value was 0.1% of the slope.

4.4.2 A Damped Sinusoidal Fit

Fitting Eq. 1.4 to the IPS position data yields a 0.1% standard deviation on the estimate of $\dot{x}(0)$ for the APPT. The present curve fitting method uses the position data 1 second prior to the pulse to obtain a small initial velocity value which is typically $< 1\%$ of $\dot{x}(0)$ and is appropriately added or subtracted from $\dot{x}(0)$. Combining the 0.1% standard deviation with the 1.7% error of the effective mass
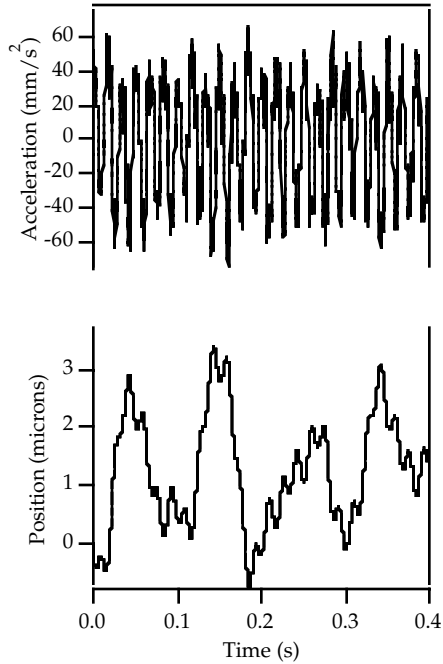
Figure 4.4: Background noise measured by IPS for pulsed gas-fed MPDT Configuration

error yields approximately 1.8% error on the APPT impulse measurement.

4.4.3 Time Resolved Acceleration

The position information obtained during the pulse of a thruster can be differentiated twice for actual acceleration information. It is necessary to first quantify the background noise in this acceleration measurement. Fig. 4.4 contains a sample of the background position data taken when the MPDT is not firing. By differentiating this data twice, the background acceleration can be quantified. Fig. 4.4 shows the results. The maximum background acceleration is 0.06 m/s^2. The power spectrum shown in Fig. 3.3 for a similar background noise measurement shows that at <5000 Hz, the acceleration amplitudes are <0.01 m/s^2. The steady state thrust for the benchmark MPDT should produce an acceleration of approximately 3 m/s^2[7]. The background noise is thus <2%.

38

Chapter 5

Experimental Results

5.1   LES 8/9 APPT

The APPT used for this experiment is the Lincoln Experimental Satellite thruster (LES-8/9)[1]. The APPT has a mass of 6.6 kg and a total impulse capability of 7320 N-s. The impulse bit is nominally 300 μN-s and the specific impulse is 1000 s. The PFN is internal and requires an external 25-150 watt power supply to charge the main 17 μF oil-filled capacitor. The pulse lasts for 5-10 μs and can pulse at a maximum of 2 Hz. The discharge occurs across the surface of a Teflon propellant bar and ablates approximately 30 μg of propellant. There are two nozzles canted at 30 degrees to the thruster axis of symmetry. For these experiments only one nozzle was fired. The APPT was mounted on the thrust stand such that the nozzle was perpendicular to the thrust arm.

On short time scales, the free-mass model for impulse bit calculations is always valid. However, it may be that the background noise disallows accurate $\dot{x}$ measurements to be made. In this case, a second alternative is to observe longer time scales and model the system with more complexity. In the case of a damped spring-mass system, Eq. 1.4 describes the dynamic response. Using the force transducer method described in section 3.3.1 and demonstrated in section 5.2 the effective mass was determined. An insert was made to fit into the nozzle and was struck at its center by the calibration pendulum. The result was m_{eff} =12.16±0.21 kg. The IPS
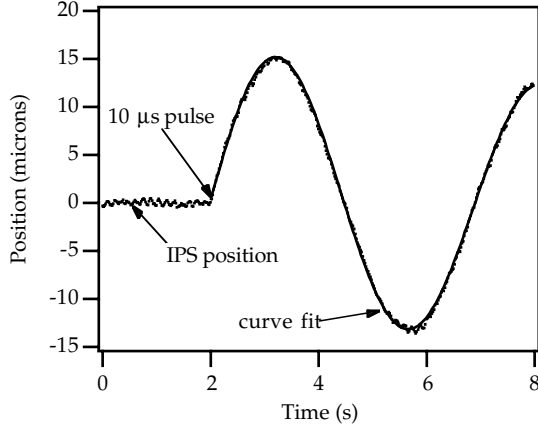
Figure 5.1: IPS position data with curve fit

configuration for the APPT experiments was also as shown in Fig. 2.1. For small damping, the maximum displacement (Δx) for this system is

$$\Delta x = \frac{2I_{bit}}{\omega_{n,eff}m_{eff}}.$$ (5.1)

Therefore, restoring forces on the thrust arm were minimized such that $\omega_{n,eff}$ was minimized and the resultant signal-to-noise ratio for position was 60:1 at maximum deflection. Section 4.4 discusses the measurement error due to background noise quantitatively. Once the effective mass is known, the position data from a damped spring-mass system can be fit to the model unambiguously. Eq. 1.4 requires ζ_{eff}, $\omega_{n,eff}$, and I_{bit} for a fit. Fig. 5.1 shows the raw, unfolded double IPS sensor position data and the curve fit. The corresponding fit values are ζ_{eff} =0.0326, $\omega_{n,eff}$ =1.279 rad/s, and I_{bit} =0.285 mN-s. The uncertainty on I_{bit} was found to be ±0.005 mN-s (1.75%).

5.2 Coaxial Quasi-Steady MPDT

5.2.1 The Quasi-Steady MPDT

The benchmark configuration[4] coaxial quasi-steady MPDT has a 12.7 cm diameter anode with a 10 cm long hemispherically tipped, 1.9 cm diameter cathode, a 5 cm

deep chamber and an anode inner radius of 5.1 cm. Propellant injection is through the back plate of the chamber. Argon at 6 g/s was used. A 1.5 ms current pulse of approximately 14 kA, shown in Fig. 5.4, is applied and the self-induced magnetic field accelerates the plasma out of the discharge chamber. The operating voltage is a nominal 100 volts.

5.2.2   Impulse Measurement

The most convenient model of the thrust stand system to use with the quasi-steady MPDT is the free-mass model. In this case Eq. 1.5 is employed and only m_{eff} needs to be determined.

The IPS was configured as shown in Fig. 2.1. The pendulum stand (see section 3.3.1 for details) was placed in front of the MPDT so that the force transducer would strike the tip of the cathode. Fig. 4.3 shows the measured force and the calculated total impulse. See Fig. 5.2 for the double sensor IPS response to the impact test. This sensor data was unfolded to produce position information and is shown in Fig. 5.3. The natural period of the thrust stand was approximately 1 second. Therefore on time scales much shorter then 1 second, the effects of the effective spring and damping are negligible. In this case m_{eff} is found from Eq. 1.5, the impulse delivered was 75.1 mN-s and thus

$$m_{eff} = \frac{I_{bit}}{\Delta \dot{x}} = \frac{75.1 \text{ mN-s}}{4.78 \text{ mm/s}} = 15.71 \pm 0.27 \text{ kg.} \tag{5.2}$$

Impulse Bit

With the IPS calibrated for this thrust stand arrangement, the quasi-steady MPDT current was pulsed as shown in the top panel of Fig. 5.4 and the IPS response was once again recorded. A slope change of 5.79 mm/s was recorded. From Eq. 1.5 and m_{eff}, the delivered impulse is

$$I_{bit} = 15.71 \text{ kg} \times 5.79 \text{ mm/s} = 0.091 \pm 0.0016 \text{ N-s.} \tag{5.3}$$
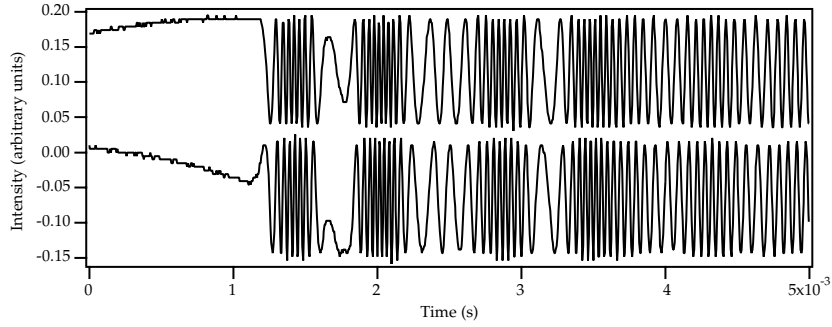
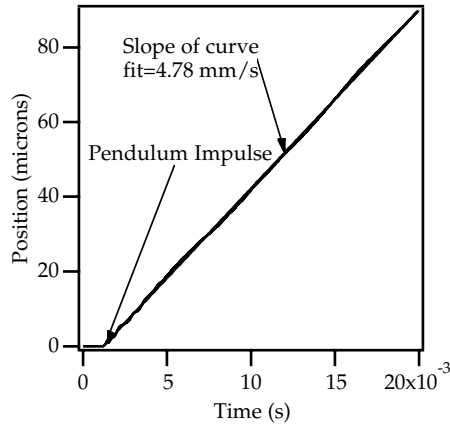Figure 5.2: Double IPS output during pendulum impact

Figure 5.3: IPS position measurement after pendulum impact

5.2.3 Instantaneous Thrust Measurement

The goal of this experiment is to demonstrate that the IPS can resolve the dynamic response of the thrust stand *during* the high power pulse of the QS-MPDT, free of EMI that plagued previous non-optical proximeters. The inference of time resolved thrust from the data proved impossible due to internal vibrations in the MPDT. Eq. 1.7 shows that if the free-mass model is accurate, only $\ddot{x}$ is needed for determining instantaneous thrust. Fig. 5.4 shows the IPS output during the pulse and demonstrates the IPS capability of recording EMI-free dynamic responses of the thruster.
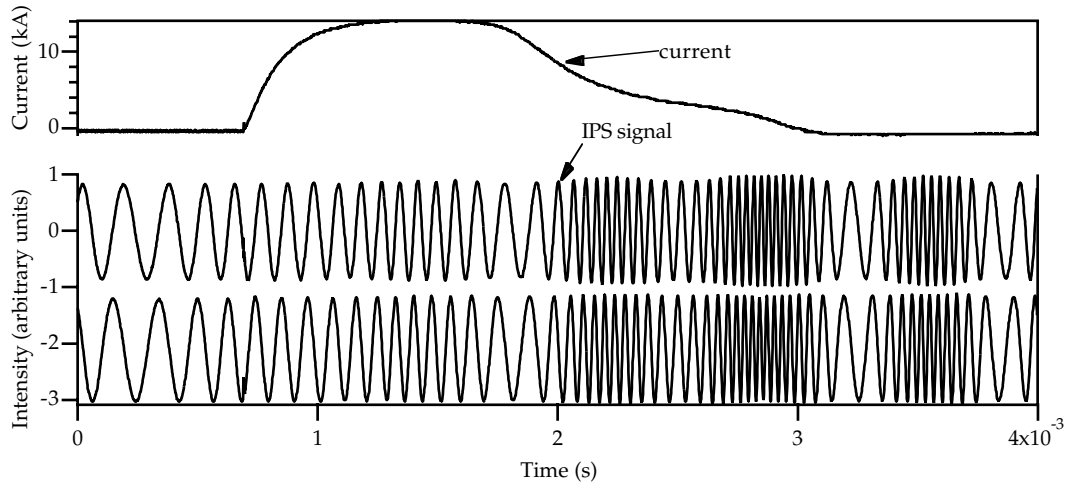
Figure 5.4: Double IPS output during a gas-fed MPD pulse

Position (x) is differentiated twice and is shown in Fig. 5.5. The acceleration error is 2% and is discussed in section 4.4.3. The $\ddot{x}$ data reveals information about the validity of the free-mass model. The actual acceleration of the thruster fluctuates. This is due to structural vibrations within the thruster and thrust arm that were excited by actuated valves and the thrust itself. Solutions to this problem include stiffening the thruster and the thrust arm. Stiffening of the thruster has been accomplished in the past[7, 8] and must be done before any attempt to extract resolved thrust information from the recorded acceleration.

5.3   Steady State Microthrust Measurement

Recent interest in steady state microthrusters ($T < 1$ mN) is accompanied by the desire to accurately measure their performance capabilities. FEEP thrusters, for example, are typically designed in the $10 - 100$ μN thrust range[21]. As described in section 3.4, the low frequency operation of the IPS can detect motion in the micron regime. Section 5.1 demonstrates this with the LES 8/9 APPT. Assuming the thruster and mounting hardware mass is less then 25 kg, a 100 μN steady state
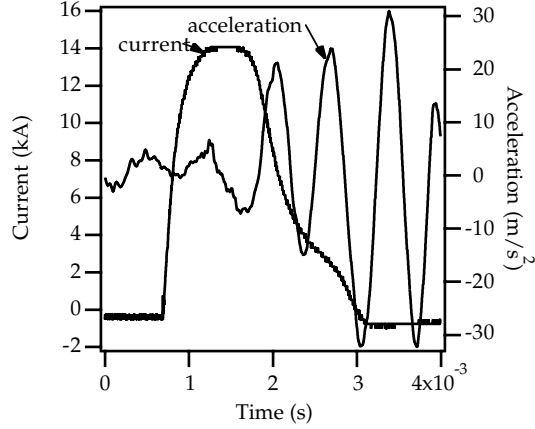
Figure 5.5: IPS $\ddot{x}$ after smoothing position

thrust lasting for 1 s will cause a displacement of approximately 15 μm. This can easily be detected by the IPS and allows a thrust measurement to be made.

Smaller thrust levels can be accommodated as well. As the thrust level drops, the thruster must be left on for a longer time to produce a measurable displacement of the thrust arm. As this time becomes comparable to the natural period of the thruster arm, the damped sinusoidal model (Eq. 1.4) becomes inappropriate. In this case, a steady state displacement method can be used. The effective spring constant on the thrust arm (k_{eff}) is easily determined from the information in section 5.1 as

$$k_{eff} = m_{eff}\omega^2 \approx 20 \ \mu\text{N}/\mu\text{m}. \tag{5.4}$$

This indicates that a 20 μN thruster will produce a steady state displacement of the thrust arm of 1 μm, a distance within the measurement capability of the IPS. By carefully aligning the thruster arm to a nearly horizontal position, the effects of gravity, which contribute to k_{eff}, have been further reduced to yield a $k_{eff} \approx 10 \ \mu\text{N}/\mu$m. It is therefore estimated that the IPS can measure microthrust levels as low as 10 μN, a range that includes many interesting microthrusters.

Conclusions

A single, high accuracy ($<2\%$ error) diagnostic was developed for thrust measurement within a very wide range of impulses (100 μN-s to above 10 N-s) covering the impulse range of all known pulsed plasma thrusters. The wide application of the thrust stand was demonstrated with thrust measurements of an ablative pulsed plasma thruster (APPT) and a quasi-steady magnetoplasmadynamic thruster (MPDT). In addition to pulsed applications, the IPS was shown to be capable of measuring *steady-state* thrust values as low as 20 μN. The NASA Jet Propulsion Laboratory has just recently (March, 1998) began conducting experiments using an IPS based thrust stand for thrust measurement of a steady state $\sim$1 mN thruster. The application of the IPS will surely be extended beyond the capabilities that were first demonstrated here.

Appendix A

Light Interference

The electric field (E_1) at a given location within a laser beam varies in time at the frequency (ω) of the laser. The magnitude of this electric field can be described by

$$E_1 = E_0 \sin(\omega t). \tag{A.1}$$

A second beam from the same source which traversed a different path in space and arrives at the same given location will produce an electric field (E_2) given by

$$E_2 = E_0 \sin(\omega t + \phi). \tag{A.2}$$

The phase of the electric field of each beam varies sinusoidally along the beam path. The difference in phase at the given location is related to L_1, L_2 and λ by

$$\phi = \frac{2\pi}{\lambda}(L_2 - L_1). \tag{A.3}$$

Adding these two electric fields at their meeting point gives an equation for the total electric field strength (E_{total}),

$$E_{total} = E_1 + E_2 = 2E_o \cos\frac{\phi}{2} \sin\left(\omega t + \frac{\phi}{2}\right) \tag{A.4}$$

The intensity of light (I) which is measured at a particular location within the fringe pattern by the photo diode, is related to the electric field strength by

$$I = \frac{E_{total}^2}{2\mu_0 c}. \tag{A.5}$$

Since the frequency of the HeNe laser light(ω) is $\sim 5 \times 10^{14}$ Hz, the time average light intensity (I_{ave}) will be the measured value due to the relatively slow frequency response of the diode (~ 100 KHz). The time average of Eqn. A.4 becomes

$$I_{ave} = \frac{2E_0^2}{\mu_0 c} \left(\frac{1}{2}\right) \cos^2 \left(\frac{\phi}{2}\right). \tag{A.6}$$

Simplifying Eqn. A.6 using a trigonometric identity yields

$$I_{ave} = \frac{E_0^2}{2\mu_0 c} \left[1 + \cos\left(\frac{2\pi}{\lambda}(L_2 - L_1)\right)\right]. \tag{A.7}$$

By normalizing Eqn. A.7 to the maximum observed intensity of the light (I_{max}), Eqn. A.7 becomes

$$I_{ave} = \frac{I_{max}}{2} \left[1 + \cos\left(\frac{2\pi}{\lambda}(L_2 - L_1)\right)\right]. \tag{A.8}$$

A change in the relative position in the x dimension of corner cube 1 with respect to corner cube 2 of δx will result in a path length change of $2\delta x$ because the light travels both to and from the corner cubes. The final dependence of the light intensity on the relative position of the corner cubes is

$$I_{ave} = \frac{I_{max}}{2} \left[1 + \cos\left(\frac{4\pi x}{\lambda}\right)\right]. \tag{A.9}$$

Appendix B

Facilities at EPPDyL

B.1 Vacuum Facilities

The vacuum vessel is a 2 m diameter, 5 m long fiberglass tank with eight optical access ports. A vacuum level on the order of 10^{-5} torr is maintained by a set of two 1.3 m diffusion pumps each with a pumping capacity of 95 m^3/s. The diffusion pumps are backed by a Roots Blower (1340 cfm) and two mechanical pumps (150 cfm).

B.2 Power Supply

The power supply consists of a 20-station 12.8 mfarad L-C PFN which can be adjusted to produce current pulses ranging from 0.5 to 2 msecs at current levels up to 50 kA. This power supply is used for the quasi-steady MPDT discussed in section 5.2. The APPT discussed in section 5.1 has internal energy storage and pulsing subsystems and requires an external 15-30 volt unregulated 30 watt power supply.

B.3 Thrust Stand Arm

The thruster is mounted on a swinging arm thrust stand. Fig. B.1 shows a gas-fed coaxial MPDT attached to the arm. The thrust arm is mounted with two flexural
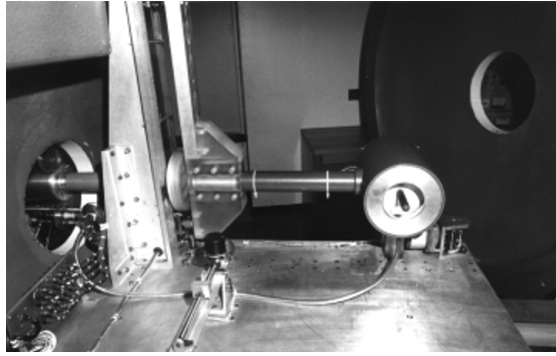
Figure B.1: The gas-fed MPD thruster and thrust stand

pivots. They are series 6016 Bendix Free-Flex Pivots[22] each with a torsional spring constant of 0.73 N-m/rad. The vertical axis of rotation of the arm can be adjusted to incorporate the force of gravity. The force of gravity can be added or subtracted from the restoring force of the flexural pivots to influence the natural period of the arm. Typical natural periods of the arm are 1-10 seconds. The thrust stand arm is fully described in Ref. [4] and is a modified version of a microthrust stand built by Fairchild Republic[12]. To reduce random mechanical perturbations to the thrust stand system, the entire thrust stand table was mechanically isolated from the tank. This was done by supporting the entire structure with springs.

Bibliography

[1] R.J. Vondra and K.I. Thomassen. Flight qualified pulsed electric thruster for satellite control. *Journal of Spacecraft and Rockets*, 11(9):613–617, September 1974.

[2] R.M. Myers and S.R. Oleson. Small satellite electric propulsion options. In *29th Intersociety Energy Conversion Engineering Conference*, Monterey, California, August 7-11 1994. AIAA 94-4137.

[3] E.Y. Choueiri. Optimization of ablative pulsed plasma thrusters for station-keeping missions. *Journal of Spacecraft and Rockets*, 33(1):96–100, 1996.

[4] R.L. Burton, K.E. Clark, and R.G. Jahn. Measured performance of a multi-megawatt MPD thruster. *Journal of Spacecraft and Rockets*, 20(3):299–304, 1983.

[5] K. Kuriki, K. Toki, and Y. Shimizu. Advanced technology experiment on-board space flyer unit (SFU), electric propulsion experiment (EPEX). Technical Report EXP-R-i003-0, Institute of Space and Astronautical Science, Tokyo, Japan, 1987.

[6] E.Y. Choueiri, A.J. Kelly, and R.G. Jahn. Mass savings domain of plasma propulsion for LEO to GEO transfer. *Journal of Spacecraft and Rockets*, 30(6):749–754, 1993.

[7] J.M. Berg, A.J. Kelly, and R.G. Jahn. Direct measurement of MPD thrust. In *17th International Electric Propulsion Conference*, Tokyo, June 27-29 1984. IEPC 84-30.

[8] K. Kuriki and H. Suzuki. Thrust measurement of quasisteady MPD. In *12th International Electric Propulsion Conference*, Key Biscayne, FL, Nov 14-17 1976. IEPC 76-1002.

[9] E.A. Cubbin, J.K. Ziemer, E.Y. Choueiri, and R.G. Jahn. Laser interferometry for pulsed plasma thruster performance measurement. In *24th International Electric Propulsion Conference*, Moscow, Russia, Sept 1995. IEPC 95-195.

[10] Research activities at the electric propulsion and plasma dynamics laboratory (EPPDyL). Progress Report EPPDyL-TR-94F, Princeton University, June-December 1994.

[11] Technical/ordering information. Technical Report L5001, Bently Nevada Corporation, April 1990.

[12] Operating instructions for plasma engine microthruster stand. Technical Report RAC 2392-1, PCD-TR-65-1, Republic Aviation Corporation, January 1965.

[13] T.W. Haag. PPT thrust stand. In *31st Joint Propulsion Conference and Exhibit*, San Diego, California, July 1995. AIAA 95-2917.

[14] Design and development of a micropound extended range thrust stand (MERTS). Technical Report NASA TN D-7029, August 1971.

[15] A.V. LaRocca and P. Malherbe. Microthrust and impulse measurement techniques for electric thrusters. In *4th Propulsion Joint Specialist Conference*, Cleveland, OH, June 10-14 1968. AIAA 68-578.

[16] T.W. Haag. Thrust stand for high power electric propulsion devices. *Review of scientific instruments*, 62(5):1186–1191, May 1991.

[17] W.T. Thomson. *Theory of Vibrations With Applications*. Prentice-Hall, Englewood Cliffs, New Jersey, 1993.

[18] G.R Fowles. *Introduction to Modern Optics*. Dover Publications Inc., New York, 1989.

[19] Technical/ordering information. Technical report, Oriel Corporation, Jan 1990.

[20] R.D. Cook and W.C. Young. *Advanced Mechanics of Materials*. Macmillan Publishing Compnay, New York, 1985.

[21] M Andrenucci. Pulsed FEEP:new experimental results. In *24th International Electric Propulsion Conference*, Moscow, Russia, September 1995. IEPC 95-97.

[22] Free flex flexural pivot engineering data. Technical Report 00U-6-681D, The Bendix Corporation-Fluid Power Division, March 1972.